

Quasi-one-dimensional spin transport in altermagnetic Z^3 nodal net metals

Tingli He,^{1,2,*} Lei Li,^{2,*} Chaoxi Cui,² Run-Wu Zhang,² Zhi-Ming Yu,² Guodong Liu,¹ and Xiaoming Zhang^{1,†}

¹*School of Materials Science and Engineering, Hebei University of Technology, Tianjin 300130, China*

²*Key Lab of advanced optoelectronic quantum architecture and measurement (MOE), Beijing Key Lab of Nanophotonics & Ultrafine Optoelectronic Systems, and School of Physics, Beijing Institute of Technology, Beijing 100081, China*

In three dimensions, quasi-one-dimensional (Q1D) transport has traditionally been associated with systems featuring a Q1D chain structure. Here, based on first-principle calculations, we go beyond the common belief to show that the Q1D transport can also be realized in many three-dimensional (3D) altermagnetic (AM) metals with a topological nodal net in momentum space but lacking Q1D chain structure in real space, including the existing compounds β -Fe₂(PO₄)O, Co₂(PO₄)O, and LiTi₂O₄. These materials exhibit an AM ground state and feature an ideal crossed Z^3 Weyl nodal line in each spin channel, formed by three straight and flat nodal lines traversing the entire Brillouin zone. These nodal lines eventually lead to an AM Z^3 nodal net. Surprisingly, longitudinal conductivity σ_{xx} in these topological nodal net metals is dozens of times larger than σ_{yy} and σ_{zz} in the up-spin channel, while σ_{yy} dominates transport in the down-spin channel. This suggests a distinctive Q1D transport signature in each spin channel, with orthogonal principal moving directions for the two spin channels, resulting in Q1D direction-dependent spin transport. This novel phenomenon cannot be found in both conventional 3D bulk materials and Q1D chain materials. In particular, it gradually disappears as the Fermi level moves away from the nodal net, further confirming its topological origin. Our work not only enhances the comprehension of topological physics in altermagnets but also opens a new direction for the exploration of topological spintronics.

The coupling of magnetism and topological states has sparked extensive research interest [1–5]. Magnetic topological materials exhibit a plethora of novel physical phenomena, including the quantum anomalous Hall effect [6–8], anomalous Hall effect [9–12], anomalous Nernst effect [12–16], and magnetoresistance effect [17, 18], which hold promising application prospects in spintronics. Magnetic ordering, on one hand, diminishes the system’s symmetry by breaking time-reversal symmetry (\mathcal{T}) and certain crystal symmetries, presenting challenges in extending topological phases to magnetic systems [19–22]. On the other hand, it introduces an additional spin degree of freedom, paving the way for achieving electric control of spin, a critical pursuit in spintronics [23–36].

In recent years, significant progress has been made in realizing various topological phases within ferromagnetic (FM) systems. Notable examples include the Co₃Sn₂S₂ [13, 37], Heusler compound Co₂MnGa [14, 38], and rutile-type metal fluorides LiV₂F₆ [39], rhombohedral transition metal trifluorides PdF₃ [12], etc. These compounds exhibit distinct physical properties within the magnetic space group, such as Weyl points and nodal lines, along with anomalous magnetic transport phenomena like the giant anomalous Hall effect and anomalous Nernst effect. Moreover, the emerging field of topological altermagnetic (AM) spintronics, facilitated by AM topological states, has garnered considerable attention [25–29]. Unlike FM systems, AM systems lack a macro-magnetic

moment, offering advantages such as eliminating stray magnetic fields, reducing power requirements, and improving operating frequency response [40–42]. Notably, various topological phases have been achieved in both AM materials and conventional antiferromagnets [43–53], paving the way for novel applications in spintronics.

A unique form of topological nodal line, termed the Z^3 nodal line, has been proposed in nonmagnetic systems [54]. Unlike conventional nodal lines, this structure traverses the entire Brillouin zone (BZ) and is characterized by three integers $Z^3 = (n_x, n_y, n_z)$, indicating the number of times the line winds around each corresponding direction [54, 55]. Remarkably, owing to significant anisotropy, the ideal Z^3 nodal line is another structure besides layered and chain structures that can lead to low-dimensional transport phenomena. Here, the “ideal” means the Z^3 nodal line is straight and has a small energy variation, as illustrated in Fig. 1. For instance, an ideal Z^3 nodal line with $n_z = 1$ would result in quasi-two-dimensional (Q2D) transport, with slower electron velocity along the z -direction compared to the x - y plane [see Fig. 1(a)]. With certain symmetries, two Z^3 nodal lines may form a crossed Z^3 nodal line, as shown in Fig. 1(b), where the y -component longitudinal conductivity will dominate the transport when the Fermi level is around the nodal line. This means that the crossed Z^3 nodal line also can lead to Q1D transport signatures. However, unlike layered and chain structures defined in real space, the Z^3 nodal line is defined in momentum space. Therefore, a natural question then is: Does an ideal Z^3 nodal line or crossed Z^3 nodal line exist in AM materials? If so, what novel transport phenomena distin-

* These authors contributed equally to this work.

† zhangxiaoming87@hebut.edu.cn

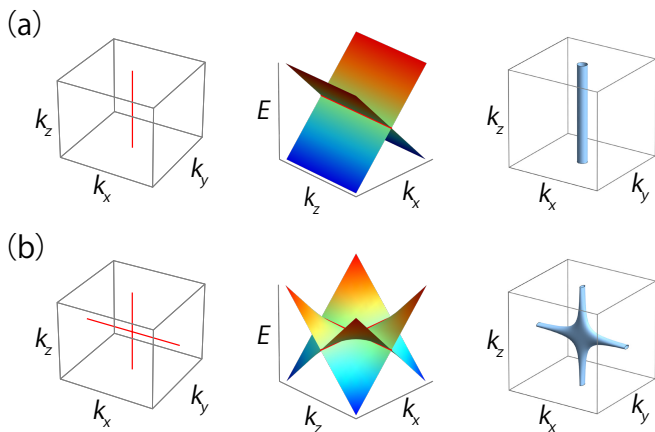


FIG. 1. Illustration of (a) an ideal Z^3 nodal line with $n_z = 1$, and (b) an ideal crossed Z^3 nodal line with $n_z = 1$ and $n_x = 1$. The figures from left to right denote the shape, the band structure and the Fermi surface of Z^3 and Z^3 crossed nodal lines. Since the Fermi surface of Z^3 and Z^3 crossed nodal lines respectively feature cylindrical and flattened shapes, the two nodal lines should exhibit Q2D and Q1D transport properties.

guish them from conventional nodal line semimetals and metals with layered or chain structures.

In this work, we demonstrate that AM materials, such as $\beta\text{-Fe}_2(\text{PO}_4)\text{O}$, $\text{Co}_2(\text{PO}_4)\text{O}$, and LiTi_2O_4 , are ideal topological Z^3 nodal net metals. Significantly, these materials deviate from conventional layered or Q1D chain materials. In these compounds, each spin channel exhibits a crossed Z^3 nodal line, formed by a Z^3 nodal line in the $k_z = 0$ plane and two Z^3 nodal lines with $n_z = 1$. At the BZ boundary, the two spin-polarized crossed nodal lines contact each other, resulting in a novel AM Z^3 nodal net configuration, as depicted in Fig. 3(c). Previous studies have elucidated the electronic structures of $\beta\text{-Fe}_2(\text{PO}_4)\text{O}$ and LiTi_2O_4 [56, 57]. Additionally, $\beta\text{-Fe}_2(\text{PO}_4)\text{O}$ has been identified as an X-type altermagnetic material [58], characterized by sublattice-selective spin-polarized transport and spin torque. However, the impact of the AM Z^3 nodal net on the spin transport properties of these systems remains unexplored.

Based on the first-principles calculations, we have discovered a class of materials characterized by novel Q1D spin transport properties. These materials exhibit an ideal Z^3 nodal net near the Fermi level. Furthermore, their longitudinal conductivity exhibits Q1D features, where the conductivity σ_{xx} (σ_{yy}) is approximately two orders of magnitude larger than σ_{yy} (σ_{xx}) and σ_{zz} in the up-spin (down-spin) channel, leading to novel Q1D direction-dependent spin transport. Notably, away from the AM Z^3 nodal net, the spin conductivity remains anisotropic but gradually loses its Q1D features, suggesting a close relationship between this novel spin transport and the AM Z^3 nodal net. To illustrate our findings, we

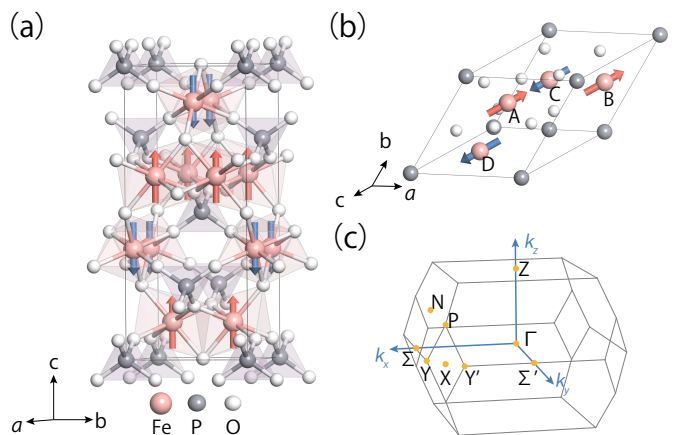


FIG. 2. (a) The conventional cell and (b) primitive cell of the $\beta\text{-Fe}_2(\text{PO}_4)\text{O}$ compound with AM ordering. Red and blue arrows represent up-spin and down-spin magnetic moments, respectively. (c) The bulk Brillouin zone (BZ) with the high symmetry points labeled.

provide concrete examples and explore their transport properties in depth.

Example 1: $\beta\text{-Fe}_2(\text{PO}_4)\text{O}$ and $\text{Co}_2(\text{PO}_4)\text{O}$.—The material $\beta\text{-Fe}_2(\text{PO}_4)\text{O}$ is a mixed-valence iron oxyphosphate featuring $\text{Fe}^{2+}/\text{Fe}^{3+}$ oxidation states [59–61]. Its single crystal was synthesized in the 1980s and experimentally confirmed to exhibit an AM phase with a Néel temperature as high as 408 K [61].

$\beta\text{-Fe}_2(\text{PO}_4)\text{O}$ crystallizes in a tetragonal Bravais lattice, as depicted in Fig. 2(a-b), displaying characteristics distinct from typical layered or chain materials. Fe and P atoms occupy the $8d$ and $4a$ Wyckoff sites, respectively, while O atoms are distributed across the $4b$ and $16h$ Wyckoff sites. Magnetic moments primarily reside on Fe sites with an approximate magnitude of $4 \mu_B$, and the Néel vector is along the z axis [see Fig. 1(a)], consistent with previous calculations [56]. The magnetic space group (MSG) for $\beta\text{-Fe}_2(\text{PO}_4)\text{O}$ is No. 141.554 ($I4'_1/am'd$). In our study, both lattice constants and atomic positions are fully relaxed. The optimized lattice parameters are found to be $a = b = 5.419 \text{ \AA}$ and $c = 12.657 \text{ \AA}$, in good agreement with experimental values ($a = b = 5.357 \text{ \AA}$ and $c = 12.505 \text{ \AA}$) [61].

Since the spin-orbit coupling (SOC) in $\beta\text{-Fe}_2(\text{PO}_4)\text{O}$ is negligible [62], we consider the spin-resolved band structure of the material without SOC, as illustrated in Fig. 3(a). In the $k_z = 0$ plane, $\beta\text{-Fe}_2(\text{PO}_4)\text{O}$ features a Z^3 Weyl nodal line in each spin channel, protected by the glide mirror symmetries $G_z = \{M_z | \frac{1}{2}0\frac{1}{2}\}$. The profiles of these two Weyl nodal lines are depicted in Fig. 3(b), showing that the Weyl nodal line in the up-spin (down-spin) channel is very straight and traverses the BZ in the k_y (k_x) direction. The two spin-resolved Weyl nodal lines contact with each other at the X point in the BZ. Fur-

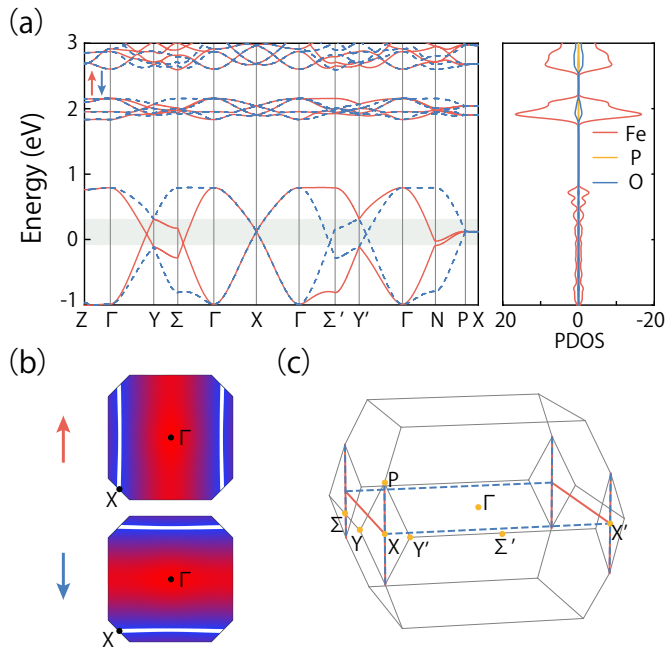


FIG. 3. (a) Electronic band structure and the projected density of states (PDOS) of $\beta\text{-Fe}_2(\text{PO}_4)\text{O}$. The energy region where the Z^3 AM nodal net appears is highlighted by green. (b) The shapes of Z^3 nodal line in each spin channel. (c) The shape of Z^3 nodal net in the BZ. Red and blue lines represent up-spin and down-spin Weyl nodal lines.

therefore, for both spin channels, the two bands around the Fermi level are degenerate along two inequivalent P - X paths, resulting in another two Z^3 nodal lines with $n_z = 1$, which are not only straight but also flat. These Z^3 nodal lines ultimately form an AM Z^3 nodal net, as depicted in Fig. 3(c).

As all the Z^3 Weyl nodal lines in $\beta\text{-Fe}_2(\text{PO}_4)\text{O}$ are ideal and exhibit an extremely strong anisotropic feature, one can expect that the longitudinal conductivity σ_{xx}^\uparrow (σ_{yy}^\downarrow) of the up-spin (down-spin) channel in this material should be much larger than σ_{yy}^\uparrow (σ_{xx}^\downarrow) and σ_{zz}^\uparrow (σ_{zz}^\downarrow). In the absence of SOC, spin serves as a good quantum number, allowing for the conductivity of up-spin and down-spin electrons to be accurately defined and calculated. Therefore, to investigate the unique Q1D direction-dependent spin transport properties of the AM Z^3 nodal net in $\beta\text{-Fe}_2(\text{PO}_4)\text{O}$, we calculate the spin-resolved longitudinal conductivities for different directions, and the obtained results are shown in Fig. 4. Three key features are observed.

Firstly, the conductivities for each spin are not independent but are connected by $C_{4z}\mathcal{T}$ symmetry, leading to $\sigma_{xx}^\uparrow = \sigma_{yy}^\downarrow$, $\sigma_{yy}^\uparrow = \sigma_{xx}^\downarrow$, and $\sigma_{zz}^\uparrow = \sigma_{zz}^\downarrow$.

Secondly, around the AM nodal net, the system's conductivity exhibits a novel spin-dependent signature where the longitudinal conductivity σ_{xx}^\uparrow (σ_{yy}^\downarrow) is dozens of times larger than the other two longitudinal conduc-

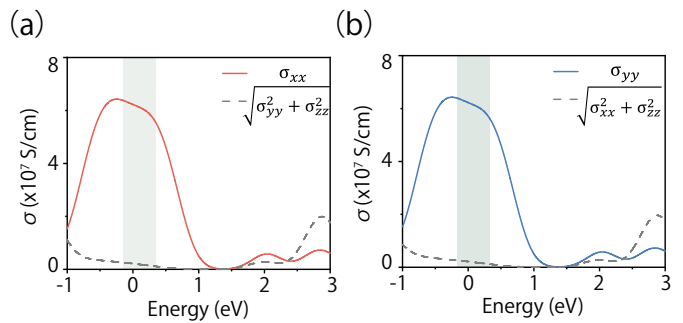


FIG. 4. The calculated conductivity of the $\beta\text{-Fe}_2(\text{PO}_4)\text{O}$ compound in (a) up-spin channel and (b) down-spin channel. The Z^3 AM nodal net appears in the green shaded region.

tivities. This implies that while the electric current is isotropic, the spin current is strongly anisotropic and shows a Q1D signature in each spin channel. This phenomenon is distinct from systems with a chain structure, where both electric and spin currents would exhibit a Q1D signature. Since the dominant transport directions for up-spin and down-spin are orthogonal, $\beta\text{-Fe}_2(\text{PO}_4)\text{O}$ can be utilized to generate a current with strong spin polarization, and the spin polarization can be easily switched by rotating the sample 90 degrees along the z axis.

Thirdly, away from the Z^3 AM nodal net, the spin conductivity remains anisotropic but progressively loses the Q1D signature. For high-energy electrons, the σ_{xx} (σ_{yy}) of the up-spin (down-spin) channel and the other two conductivities are of the same order of magnitude (see Fig. 4). This strongly suggests that the spin-polarized Q1D transport is closely associated with the Z^3 nodal net rather than the system's structure.

The synthesis of $\text{Co}_2(\text{PO}_4)\text{O}$ has also been reported [63], showing a similar crystalline structure, magnetic configuration, and electronic band properties as $\beta\text{-Fe}_2(\text{PO}_4)\text{O}$ [62]. Notably, the Q1D spin transport signature is also significant in $\text{Co}_2(\text{PO}_4)\text{O}$. Further details can be found in Ref. [62].

Example 2: LiTi_2O_4 .—In addition to the $\beta\text{-Fe}_2(\text{PO}_4)\text{O}$ compound, the LiTi_2O_4 compound also exhibits an AM Z^3 nodal net near the Fermi level. The lattice structure of LiTi_2O_4 , depicted in Fig. 5(a), belongs to a cubic Bravais lattice, which differs from that of $\beta\text{-Fe}_2(\text{PO}_4)\text{O}$. The AM ground state of LiTi_2O_4 is characterized by a magnetic symmetry of $141.554 (I4_1/am'd)$ [57].

The SOC effect in LiTi_2O_4 is also negligible. Figure 5(c) illustrates the spin-resolved band structure of LiTi_2O_4 in the absence of SOC. Scanning through the Brillouin zone (BZ) reveals the profile of the AM Z^3 nodal net, as depicted in Fig. 5(b). This AM nodal net configuration consists of one nodal line in the $k_z = 0$ plane and two nodal lines along two inequivalent P - X paths for each spin channel. The obtained spin longitudi-

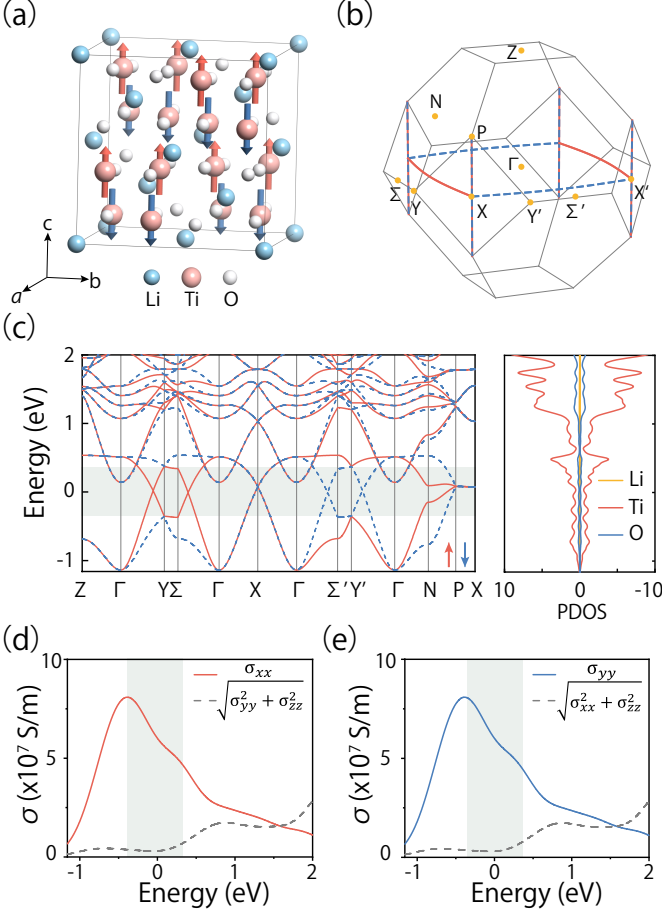


FIG. 5. (a) Crystal structures of the LiTi_2O_4 compound. Red and blue arrows represent up-spin and down-spin magnetic moments, respectively. (b) BZ and the shape of the Z^3 nodal net. Red and blue lines represent up-spin and down-spin Weyl nodal lines. (c) Electronic band structure and the PDOS of LiTi_2O_4 compound. The calculated conductivity in (d) up-spin channel and (e) down-spin channel. The Z^3 AM nodal net appears in the green shaded region.

nal conductivities are displayed in Fig. 5(d-e), exhibiting similar features to those observed in $\beta\text{-Fe}_2(\text{PO}_4)\text{O}$ and $\text{Co}_2(\text{PO}_4)\text{O}$. This further confirms that Q1D spin transport is a common characteristic of materials possessing an ideal Z^3 nodal net.

Lattice model of AM Z^3 nodal net.— To further understand the Q1D spin transport, we establish a simple effective lattice model for the AM Z^3 nodal net, based on $\beta\text{-Fe}_2(\text{PO}_4)\text{O}$. We consider a 3D tetragonal body-centred lattice with an AM ordering, and assume that this lattice has the same MSG (No. 141.554) as the $\beta\text{-Fe}_2(\text{PO}_4)\text{O}$. The unit cell of the antiferromagnet includes an even number of lattice sites: up spins on half of sites and down spins on the remaining half. The lattice has four atoms with s -like orbitals per unit cell at $8d$ Wyckoff sites (labeled as $\{A, B, C, D\}$), which correspond to the positions occupied by the Fe atoms of $\beta\text{-Fe}_2(\text{PO}_4)\text{O}$ [see Fig. 2(b)].

The lattice has space group (SG) symmetry D_{4h}^{19} (e.g. the SG 141), which is generated by a four-fold screw-rotation $S_{4z} = \{C_{4z} | \frac{1}{4} \frac{-1}{4} \frac{1}{4}\}$, a two-fold rotation C_{2x} and a spatial inversion P . Combining S_{4z}^2 and P leads to a glide mirror plane $G_z = \{M_z | \frac{1}{2} 0 \frac{1}{2}\}$. Without alternating magnetic ordering, the lattice also has time-reversal symmetry \mathcal{T} . In the absence of SOC, using the four sites as a basis, the symmetry operators can be represented as

$$S_{4z} = \begin{bmatrix} 0 & 0 & 1 & 0 \\ 0 & 0 & 0 & 1 \\ 0 & 1 & 0 & 0 \\ 1 & 0 & 0 & 0 \end{bmatrix}, C_{2x} = \begin{bmatrix} 1 & 0 & 0 & 0 \\ 0 & 1 & 0 & 0 \\ 0 & 0 & 0 & 1 \\ 0 & 0 & 1 & 0 \end{bmatrix}, \quad (1)$$

$P = \Gamma_{0,0}$ and $\mathcal{T} = \Gamma_{0,0}\mathcal{K}$ with $\Gamma_{i,j} = \sigma_i \otimes \sigma_j$. Here, σ_0 is identity matrix and σ denote the Pauli matrixes. The corresponding model Hamiltonian under these symmetry constraints may be written as [64, 65]

$$\mathcal{H}_0 = \begin{bmatrix} H_1 & H' \\ H'^{\dagger} & H_2 \end{bmatrix}, \quad (2)$$

where $H_1 = t_1 \cos \frac{k_x + k_z}{2} \sigma_1$, $H_2 = t_1 \cos \frac{k_y + k_z}{2} \sigma_1$ and

$$H' = t_2 \begin{bmatrix} \cos \frac{k_z}{2} & \cos \frac{k_y}{2} \\ \cos \frac{k_x}{2} & \cos \frac{k_x + k_y + k_z}{2} \end{bmatrix}, \quad (3)$$

with t_i ($i = 1, 2$) the real parameters.

Then, we introduce spin degree of freedom and turn on a AM ordering along z -direction [see Fig. 2(a)]. The AM ordering breaks \mathcal{T} , S_{4z} and C_{2x} , while holds G_z , S_{2z} , P and the combined operation $S_{4z}\mathcal{T}$ and $C_{2x}\mathcal{T}$. To the leading order, the AM Hamiltonian may be written as

$$\mathcal{H} = \mathcal{H}_0 s_0 + J_z s_z \Gamma_{3,0}, \quad (4)$$

with \mathbf{s} the Pauli matrixes acting on spin space and J_z denoting the strength of the AM potential. When the AM potential ($J_z > 0$) is much stronger than other hopping and energy terms, the eight bands are divided into two groups with each group including four bands. Since the two groups are separated in energy space by $2J_z$, the model (4) can be simplified as two effectively four-band model [66]. The basis of the upper subsystem is $(|A \uparrow\rangle, |B \uparrow\rangle, |C \downarrow\rangle, |D \downarrow\rangle)^T$ and that for the lower subsystem is $(|A \downarrow\rangle, |B \downarrow\rangle, |C \uparrow\rangle, |D \uparrow\rangle)^T$. We focus on the upper subsystem and omit J_z from it, as it only shifts the bands. Following the classical method [67], the upper four-band model can be expressed as

$$\mathcal{H}_{\text{eff}} = \frac{t_2^2}{4J_z} + \begin{bmatrix} H_1 & 0 \\ 0 & H_2 \end{bmatrix} + \frac{t_2^2}{4J_z} \begin{bmatrix} H'_1 & 0 \\ 0 & H'_2 \end{bmatrix}, \quad (5)$$

with

$$H'_1(\mathbf{k}) = 2\left(\cos \frac{k_x}{2} \cos \frac{k_z}{2} + \cos \frac{k_y}{2} \cos \frac{k_x + k_y + k_z}{2}\right)\sigma_1 + \begin{bmatrix} \cos k_y + \cos k_z & 0 \\ 0 & \cos k_x + \cos(k_x + k_y + k_z) \end{bmatrix},$$

and $H'_2(k_x, k_y, k_z) = H'_1(k_y, k_x, k_z)$.

The band structure of \mathcal{H}_{eff} is calculated and plotted in Ref. [62], which qualitatively reproduces the band structure of $\beta\text{-Fe}_2(\text{PO}_4)\text{O}$. Our simple four-band effective model hence can serve as a good starting point for the further study of the physics of AM Z^3 nodal net.

Conclusions.—In conclusion, we have demonstrated the feasibility of achieving the ideal AM Z^3 nodal net in real materials and shown that the novel Q1D spin transport phenomena inherent to this topological structure. We have detailed the mechanisms whereby electrons with up-spin predominantly flow in one direction, while those with down-spin move primarily in a perpendicular direction, a characteristic distinctly contrasting with conventional 3D bulk materials and Q1D chain materials. This behavior could be effectively detected through the measurement of anisotropic spin resistance, offering a practical approach to exploring the unique physics of AM systems. Our work not only provides a solid foundation for exploring the novel physics of AM systems but also holds great promise for applications in topological spintronics.

-
- [1] J. Kruthoff, J. de Boer, J. van Wezel, C. L. Kane, and R.-J. Slager, Topological classification of crystalline insulators through band structure combinatorics, *Phys. Rev. X* **7**, 041069 (2017).
- [2] Y. Tokura, K. Yasuda, and A. Tsukazaki, Magnetic topological insulators, *Nat. Rev. Phys.* **1**, 126 (2019).
- [3] Y. Xu, L. Elcoro, Z.-D. Song, B. J. Wieder, M. G. Vergniory, N. Regnault, Y. Chen, C. Felser, and B. A. Bernevig, High-throughput calculations of magnetic topological materials, *Nature* **586**, 702 (2020).
- [4] L. Elcoro, B. J. Wieder, Z. Song, Y. Xu, B. Bradlyn, and B. A. Bernevig, Magnetic topological quantum chemistry, *Nat. Commun.* **12**, 5965 (2021).
- [5] B. A. Bernevig, C. Felser, and H. Beidenkopf, Progress and prospects in magnetic topological materials, *Nature* **603**, 41 (2022).
- [6] H. Sun, B. Xia, Z. Chen, Y. Zhang, P. Liu, Q. Yao, H. Tang, Y. Zhao, H. Xu, and Q. Liu, Rational design principles of the quantum anomalous hall effect in superlattice-like magnetic topological insulators, *Phys. Rev. Lett.* **123**, 096401 (2019).
- [7] Y. Deng, Y. Yu, M. Z. Shi, Z. Guo, Z. Xu, J. Wang, X. H. Chen, and Y. Zhang, Quantum anomalous Hall effect in intrinsic magnetic topological insulator MnBi_2Te_4 , *Science* **367**, 895 (2020).
- [8] H. Li, C.-Z. Chen, H. Jiang, and X. C. Xie, Coexistence of Quantum Hall and Quantum Anomalous Hall Phases in Disordered MnBi_2Te_4 , *Phys. Rev. Lett.* **127**, 236402 (2021).
- [9] H. Chen, Q. Niu, and A. H. MacDonald, Anomalous hall effect arising from noncollinear antiferromagnetism, *Phys. Rev. Lett.* **112**, 017205 (2014).
- [10] Y. Zhang, Y. Sun, H. Yang, J. Železný, S. P. P. Parkin, C. Felser, and B. Yan, Strong anisotropic anomalous Hall effect and spin Hall effect in the chiral antiferromagnetic compounds Mn_3X ($X = \text{Ge}, \text{Sn}, \text{Ga}, \text{Ir}, \text{Rh}, \text{and Pt}$), *Phys. Rev. B* **95**, 075128 (2017).
- [11] P. Li, J. Koo, W. Ning, J. Li, L. Miao, L. Min, Y. Zhu, Y. Wang, N. Alem, C.-X. Liu, Z. Mao, and B. Yan, Giant room temperature anomalous Hall effect and tunable topology in a ferromagnetic topological semimetal Co_2MnAl , *Nat. Commun.* **11**, 3476 (2020).
- [12] X. Zhou, R.-W. Zhang, X. Yang, X.-P. Li, W. Feng, Y. Mokrousov, and Y. Yao, Disorder- and topology-enhanced fully spin-polarized currents in nodal chain spin-gapless semimetals, *Phys. Rev. Lett.* **129**, 097201 (2022).
- [13] S. N. Guin, P. Vir, Y. Zhang, N. Kumar, S. J. Watzman, C. Fu, E. Liu, K. Manna, W. Schnelle, J. Gooth, *et al.*, Zero-Field Nernst Effect in a Ferromagnetic Kagome-Lattice Weyl-Semimetal $\text{Co}_3\text{Sn}_2\text{S}_2$, *Adv. Mater.* **31**, 1806622 (2019).
- [14] S. N. Guin, K. Manna, J. Noky, S. J. Watzman, C. Fu, N. Kumar, W. Schnelle, C. Shekhar, Y. Sun, J. Gooth, *et al.*, Anomalous Nernst effect beyond the magnetization scaling relation in the ferromagnetic Heusler compound Co_2MnGa , *NPG Asia Mater.* **11**, 16 (2019).
- [15] H. Zhang, C. Q. Xu, and X. Ke, Topological Nernst effect, anomalous Nernst effect, and anomalous thermal Hall effect in the Dirac semimetal Fe_3Sn_2 , *Phys. Rev. B* **103**, L201101 (2021).
- [16] Y. Pan, C. Le, B. He, S. J. Watzman, M. Yao, J. Gooth, J. P. Heremans, Y. Sun, and C. Felser, Giant anomalous Nernst signal in the antiferromagnet YbMnBi_2 , *Nat. Mater.* **21**, 203 (2022).
- [17] T. Suzuki, L. Savary, J.-P. Liu, J. W. Lynn, L. Balents, and J. G. Checkelsky, Singular angular magnetoresistance in a magnetic nodal semimetal, *Science* **365**, 377 (2019).
- [18] Y. Zhu, C.-Y. Huang, Y. Wang, D. Graf, H. Lin, S. H. Lee, J. Singleton, L. Min, J. C. Palmstrom, A. Bansil, B. Singh, and Z. Mao, Large anomalous Hall effect and negative magnetoresistance in half-topological semimetals, *Commun. Phys.* **6**, 346 (2023).
- [19] Z.-M. Yu, Z. Zhang, G.-B. Liu, W. Wu, X.-P. Li, R.-W. Zhang, S. A. Yang, and Y. Yao, Encyclopedia of emergent particles in three-dimensional crystals, *Sci. Bull.* **67**, 375 (2022).
- [20] Z. Zhang, G.-B. Liu, Z.-M. Yu, S. A. Yang, and Y. Yao, Encyclopedia of emergent particles in type-iv magnetic space groups, *Phys. Rev. B* **105**, 104426 (2022).
- [21] G.-B. Liu, Z. Zhang, Z.-M. Yu, S. A. Yang, and Y. Yao, Systematic investigation of emergent particles in type-iii magnetic space groups, *Phys. Rev. B* **105**, 085117 (2022).
- [22] Z. Zhang, Z.-M. Yu, and S. A. Yang, Magnetic higher-order nodal lines, *Phys. Rev. B* **103**, 115112 (2021).
- [23] H. Yan, Z. Feng, P. Qin, X. Zhou, H. Guo, X. Wang, H. Chen, X. Zhang, H. Wu, C. Jiang, and Z. Liu, Electric-Field-Controlled Antiferromagnetic Spintronic Devices, *Adv. Mater.* **32**, 1905603 (2020).
- [24] S. K. Kim, G. S. Beach, K.-J. Lee, T. Ono, T. Rasing, and H. Yang, Ferrimagnetic spintronics, *Nat. Mater.* **21**, 24 (2022).
- [25] R. González-Hernández, L. Šmejkal, K. Výborný, Y. Yahagi, J. Sinova, T. c. v. Jungwirth, and J. Železný, Efficient Electrical Spin Splitter Based on Nonrelativistic Collinear Antiferromagnetism, *Phys. Rev. Lett.* **126**, 127701 (2021).
- [26] L. Šmejkal, A. B. Hellenes, R. González-Hernández,

- J. Sinova, and T. Jungwirth, Giant and tunneling magnetoresistance in unconventional collinear antiferromagnets with nonrelativistic spin-momentum coupling, *Phys. Rev. X* **12**, 011028 (2022).
- [27] H. Chen, L. Liu, X. Zhou, Z. Meng, X. Wang, Z. Duan, G. Zhao, H. Yan, P. Qin, and Z. Liu, Emerging antiferromagnets for spintronics, *Adv. Mater.*, 2310379 (2024).
- [28] L. Šmejkal, J. Sinova, and T. Jungwirth, Beyond conventional ferromagnetism and antiferromagnetism: A phase with nonrelativistic spin and crystal rotation symmetry, *Phys. Rev. X* **12**, 031042 (2022).
- [29] L. Šmejkal, J. Sinova, and T. Jungwirth, Emerging research landscape of altermagnetism, *Phys. Rev. X* **12**, 040501 (2022).
- [30] S. Hu, D.-F. Shao, H. Yang, C. Pan, Z. Fu, M. Tang, Y. Yang, W. Fan, S. Zhou, E. Y. Tsymbal, *et al.*, Efficient perpendicular magnetization switching by a magnetic spin hall effect in a noncollinear antiferromagnet, *Nat. Commun.* **13**, 4447 (2022).
- [31] D.-F. Shao, Y.-Y. Jiang, J. Ding, S.-H. Zhang, Z.-A. Wang, R.-C. Xiao, G. Gurung, W. J. Lu, Y. P. Sun, and E. Y. Tsymbal, Néel Spin Currents in Antiferromagnets, *Phys. Rev. Lett.* **130**, 216702 (2023).
- [32] D.-F. Shao and E. Y. Tsymbal, Antiferromagnetic tunnel junctions for spintronics, *arXiv preprint arXiv:2312.13507* (2023).
- [33] Z. Feng, H. Yan, and Z. Liu, Electric-Field Control of Magnetic Order: From FeRh to Topological Antiferromagnetic Spintronics, *Adv. Electron. Mater.* **5**, 1800466 (2019).
- [34] H. Tsai, T. Higo, K. Kondou, T. Nomoto, A. Sakai, A. Kobayashi, T. Nakano, K. Yakushiji, R. Arita, S. Miwa, Y. Otani, and S. Nakatsuji, Electrical manipulation of a topological antiferromagnetic state, *Nature* **580**, 608–613 (2020).
- [35] R.-W. Zhang, C. Cui, R. Li, J. Duan, L. Li, Z.-M. Yu, and Y. Yao, Predictable gate-field control of spin in altermagnets with spin-layer coupling, *arXiv preprint arXiv:2306.08902* (2023).
- [36] J. Gong, Y. Wang, Y. Han, Z. Cheng, X. Wang, Z.-M. Yu, and Y. Yao, Hidden Real Topology and Unusual Magnetoelectric Responses in Monolayer Antiferromagnetic Cr₂Se₂O, *arXiv preprint arXiv:2310.20510* (2023).
- [37] Q. Wang, Y. Xu, R. Lou, Z. Liu, M. Li, Y. Huang, D. Shen, H. Weng, S. Wang, and H. Lei, Large intrinsic anomalous Hall effect in half-metallic ferromagnet Co₃Sn₂S₂ with magnetic Weyl fermions **9**, 10.1038/s41467-018-06088-2.
- [38] G. Chang, S.-Y. Xu, X. Zhou, S.-M. Huang, B. Singh, B. Wang, I. Belopolski, J. Yin, S. Zhang, A. Bansil, H. Lin, and M. Z. Hasan, Topological Hopf and Chain Link Semimetal States and Their Application to Co₂MnGa, *Phys. Rev. Lett.* **119**, 156401 (2017).
- [39] R.-W. Zhang, X. Zhou, Z. Zhang, D.-S. Ma, Z.-M. Yu, W. Feng, and Y. Yao, Weyl monoloop semi-half-metal and tunable anomalous hall effect, *Nano Lett.* **21**, 8749 (2021).
- [40] T. Jungwirth, X. Marti, P. Wadley, and J. Wunderlich, Antiferromagnetic spintronics, *Nat. Nanotechnol.* **11**, 231 (2016).
- [41] V. Baltz, A. Manchon, M. Tsoi, T. Moriyama, T. Ono, and Y. Tserkovnyak, Antiferromagnetic spintronics, *Rev. Mod. Phys.* **90**, 015005 (2018).
- [42] L. Šmejkal, Y. Mokrousov, B. Yan, and A. H. MacDonald, Topological antiferromagnetic spintronics, *Nat. Phys.* **14**, 242 (2018).
- [43] P. Tang, Q. Zhou, G. Xu, and S.-C. Zhang, Dirac fermions in an antiferromagnetic semimetal, *Nat. Phys.* **12**, 1100 (2016).
- [44] G. Hua, S. Nie, Z. Song, R. Yu, G. Xu, and K. Yao, Dirac semimetal in type-IV magnetic space groups, *Phys. Rev. B* **98**, 201116 (2018).
- [45] B. Wang, H. Gao, Q. Lu, W. Xie, Y. Ge, Y.-H. Zhao, K. Zhang, and Y. Liu, Type-I and type-II nodal lines coexistence in the antiferromagnetic monolayer CrAs₂, *Phys. Rev. B* **98**, 115164 (2018).
- [46] J. Liu and L. Balents, Anomalous Hall Effect and Topological Defects in Antiferromagnetic Weyl Semimetals: Mn₃Sn/Ge, *Phys. Rev. Lett.* **119**, 087202 (2017).
- [47] M. Yang, Y. Qian, D. Yan, Y. Li, Y. Song, Z. Wang, C. Yi, H. L. Feng, H. Weng, and Y. Shi, Magnetic and electronic properties of a topological nodal line semimetal candidate: HoSbTe, *Phys. Rev. Mater.* **4**, 094203 (2020).
- [48] D.-F. Shao, G. Gurung, S.-H. Zhang, and E. Y. Tsymbal, Dirac nodal line metal for topological antiferromagnetic spintronics, *Phys. Rev. Lett.* **122**, 077203 (2019).
- [49] S. Malick, J. Singh, A. Laha, V. Kanchana, Z. Hossain, and D. Kaczorowski, Electronic structure and physical properties of EuAuAs single crystal, *Phys. Rev. B* **105**, 045103 (2022).
- [50] L. Huang, J. Zhu, W. Wu, J. Cao, Z. Zhang, Y. Jiao, Y. Liu, L. Wang, and S. A. Yang, Antiferromagnetic nodal loop and strain-controllable magnetic phase transition in monolayer MnAl, *Appl. Phys. Lett.* **121**, 213101 (2022).
- [51] J. Zhan, J. Li, W. Shi, X.-Q. Chen, and Y. Sun, Coexistence of weyl semimetal and weyl nodal loop semimetal phases in a collinear antiferromagnet, *Phys. Rev. B* **107**, 224402 (2023).
- [52] T. P. T. Nguyen and K. Yamauchi, Ab initio prediction of anomalous Hall effect in antiferromagnetic CaCrO₃, *Phys. Rev. B* **107**, 155126 (2023).
- [53] Z. Zhu, H. Liu, Y. Ge, Z. Zhang, W. Wu, C. Xiao, and S. A. Yang, Third-order charge transport in a magnetic topological semimetal, *Phys. Rev. B* **107**, 205120 (2023).
- [54] S. Li, Z.-M. Yu, Y. Liu, S. Guan, S.-S. Wang, X. Zhang, Y. Yao, and S. A. Yang, Type-ii nodal loops: Theory and material realization, *Phys. Rev. B* **96**, 081106 (2017).
- [55] Z.-M. Yu, W. Wu, X.-L. Sheng, Y. X. Zhao, and S. A. Yang, Quadratic and cubic nodal lines stabilized by crystalline symmetry, *Phys. Rev. B* **99**, 121106 (2019).
- [56] T. He, X. Zhang, W. Meng, L. Jin, X. Dai, and G. Liu, Topological nodal lines and nodal points in the antiferromagnetic material β -Fe₂PO₅, *J. Mater. Chem. C* **7**, 12657 (2019).
- [57] T. He, X. Zhang, Y. Liu, X. Dai, L. Wang, and G. Liu, Potential antiferromagnetic Weyl nodal line state in LiTi₂O₄ material, *Phys. Rev. B* **104**, 045143 (2021).
- [58] S.-S. Zhang, Z.-A. Wang, B. Li, S.-H. Zhang, R.-C. Xiao, L.-X. Liu, X. Luo, W. Lu, M. Tian, Y. Sun, *et al.*, X-type antiferromagnets, *arXiv preprint arXiv:2310.13271* (2023).
- [59] A. Modaresi, A. Courtois, R. Gerardin, B. Malaman, and C. Gleitzer, Fe₂PO₅, un phosphate de fer de valence mixte. Préparation et études structurale, mössbauer et magnétique, *J. Solid State Chem.* **40**, 301 (1981).
- [60] B. Ech-Chahed, F. Jeannot, B. Malaman, and C. Gleitzer, Préparation et étude d'une variété basse

- tempe´rature de l’oxyphosphate de fer de valence mixte β -Fe₂(PO₄)O et de NiCr(PO₄)O: Un cas d’e´changee´lectronique rapide, *J. Solid State Chem.* **74**, 47 (1988).
- [61] M. Ijjaali, B. Malaman, C. Gleitzer, J. Warner, J. Hriljac, and A. Cheetham, Stability, structure refinement, and magnetic properties of β -Fe₂(PO₄)O, *J. Solid State Chem.* **86**, 195 (1990).
- [62] See Supplemental Material for the calculation methods, the band structure of the β -Fe₂(PO₄)O compound with spin-orbit coupling, detailed analysis of the Co₂(PO₄)O compound, and the band structure of the lattice model.
- [63] G. Wang, M. Valldor, E. T. Spielberg, and A.-V. Mudring, Ionothermal Synthesis, Crystal Structure, and Magnetic Study of Co₂PO₄OH Isostructural with Caminite, *Inorg. Chem.* **53**, 3072 (2014).
- [64] Z. Zhang, Z.-M. Yu, G.-B. Liu, and Y. Yao, MagneticTB: A package for tight-binding model of magnetic and non-magnetic materials, *Comput. Phys. Commun.* **270**, 108153 (2022).
- [65] Z. Zhang, Z.-M. Yu, G.-B. Liu, Z. Li, S. A. Yang, and Y. Yao, MagneticKP: A package for quickly constructing $k \cdot p$ models of magnetic and non-magnetic crystals, *Comput. Phys. Commun.* **290**, 108784 (2023).
- [66] J. Wang, Antiferromagnetic dirac semimetals in two dimensions, *Phys. Rev. B* **95**, 115138 (2017).
- [67] R. Winkler, S. Papadakis, E. De Poortere, and M. Shayegan, *Spin-orbit coupling in two-dimensional electron and hole systems*, Vol. 41 (Springer, 2003).

Supplemental Material for “ Quasi-one-dimensional spin transport in antiferromagnetic Z^3 nodal net metals ”

Tingli He,^{1,2} Lei Li,² Chaoxi Cui,² Run-Wu Zhang,² Zhi-Ming Yu,² Guodong Liu,¹ and Xiaoming Zhang¹

¹*School of Materials Science and Engineering, Hebei University of Technology, Tianjin 300130, China*

²*Key Lab of advanced optoelectronic quantum architecture and measurement (MOE), Beijing Key Lab of Nanophotonics & Ultrafine Optoelectronic Systems, and School of Physics, Beijing Institute of Technology, Beijing 100081, China*

I. CALCULATION METHODS

The first-principles calculations in the work are based on the density functional theory (DFT) using the Vienna ab initio Simulation Package [1, 2]. The generalized gradient approximation (GGA) of the Perdew-BurkeErnzerhof (PBE) functional was modeled as the exchange-correlation potential [3]. The cutoff energy was set at 500 eV, and a Monkhorst-Pack k -point mesh of $15 \times 15 \times 15$ was used for the Brillouin zone (BZ) sampling [4]. The energy and force convergence criteria were set as 10^{-7} eV and 0.001 eV/Å in the calculation. The GGA + U method was employed to describe the strongly correlated Fe $3d$ orbitals [5, 6]. The effective U value of Fe and Ti atom were set to 4 eV, Co was set to 3 eV. The electrical conductivity was calculated using the Boltzmann equation in the Wannier90 code [7, 8], employing a $100 \times 100 \times 100$ crystal momentum mesh and a relaxation time τ of 500 fs ($\Gamma = 8.27$ meV).

II. BAND STRUCTURE WITH THE SPIN-ORBIT COUPLING INCLUDED OF β -Fe₂(PO₄)O

The band structure with spin-orbit coupling (SOC) included is shown in Fig. S1 for the β -Fe₂(PO₄)O compound. One can see that the two spin channels are coupled, but the band crossings are still maintained. Due to the weak SOC effect of the system, only a small band gap opens up on the X point. Therefore, we mainly discussed the results of β -Fe₂(PO₄)O compound without SOC in the main text.

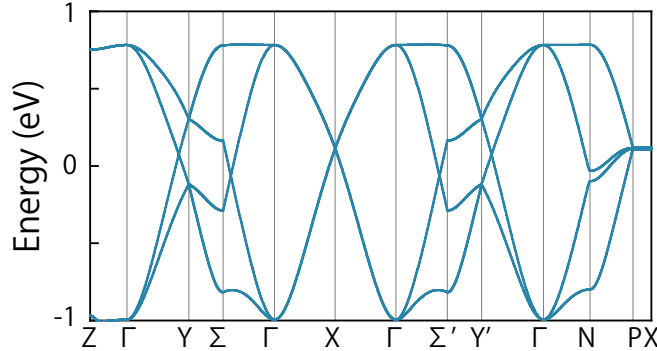


FIG. S1: The band structure with the SOC included of β -Fe₂(PO₄)O compound.

III. DETAILED ANALYSIS OF THE CO₂(PO₄)O COMPOUND

The Co₂(PO₄)O compound has a tetragonal Bravais lattice, as shown in Fig. S2(a). The Co₂(PO₄)O compound has a similar Z^3 nodal net near the Fermi level under the antiferromagnetic (AM) ground state. The spin-resolved band structure and projected density of states (PDOS) without SOC are shown in Fig. S2(c). The corresponding k -paths are displayed in Fig. S2(b). In the $k_z = 0$ plane, Co₂(PO₄)O has a Z^3 Weyl nodal line in each spin channel, which is protected by mirror symmetries. The two spin-resolved Weyl nodal lines contact with each other at the X point in the BZ [see the Fig. S2(b)]. Moreover, around the Fermi level, the two bands of each spin channel are degenerate along the P - X path, leading to another two Z^3 nodal lines with $n_z = 1$, which are not only straight but also flat. These Z^3 nodal lines eventually form a Z^3 AM nodal net, as shown in Fig. S2(b).

The conductivity of different spin channels are shown in Fig. S2(d-e). One can observe that the longitudinal conductivity σ_{xx}^\uparrow (σ_{yy}^\downarrow) is dozens of times larger than the other two longitudinal conductivities. Near the Fermi level, σ_{xx} dominates transport in the up-spin channel, while σ_{yy} dominates transport in the down-spin channel, leading to novel Q1D direction-dependent spin transport. However, moving away from the nodal line will result in the loss of these Q1D direction-dependent transport properties. This strongly indicates that the Q1D spin transport is caused by the AM Z^3 nodal net. It can be believed that similar structures such as $M_2PO_4O(F)$ ($M = \text{Metal}$) can also exhibit similar Z^3 nodal nets. If the ideal Z^3 nodal net is near the Fermi level, the system will have novel low-dimensional transport properties.

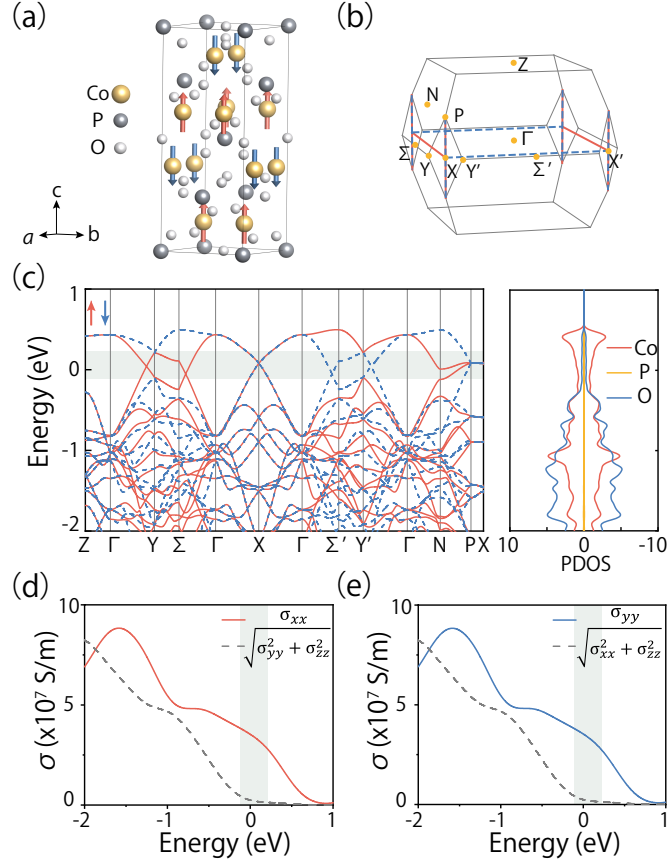


FIG. S2: (a) Crystal structures of $\text{Co}_2(\text{PO}_4)\text{O}$ compound. Red and blue arrows represent up-spin and down-spin magnetic moments, respectively. (b) The shape of Z^3 nodal net in the BZ. Red and blue lines represent up-spin and down-spin Weyl nodal lines. (c) Electronic band structure and the projected density of states PDOS of $\text{Co}_2(\text{PO}_4)\text{O}$ compound. The Calculated conductivity of $\text{Co}_2(\text{PO}_4)\text{O}$ in (d) up-spin channel and (e) down-spin channel. The Z^3 AM nodal net appears in the green shaded region.

IV. THE BAND STRUCTURE OF LATTICE MODEL

The band structure of \mathcal{H}_{eff} in the main text is shown in the Fig. S3, which qualitatively reproduces the band structure of $\beta\text{-Fe}_2(\text{PO}_4)\text{O}$.

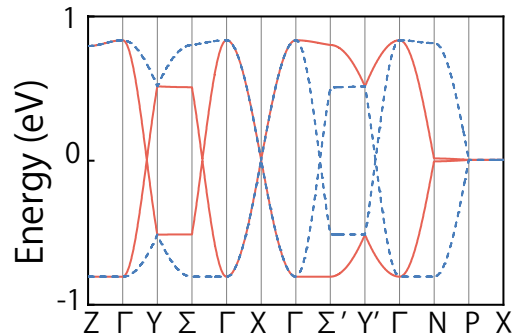


FIG. S3: Calculated electronic band structure of \mathcal{H}_{eff} in the main text with $t_1 = 0.8$, $t_2 = 0.2$, $J_z = 2$. The up-spin and down-spin bands are denoted by red and blue curves.

-
- [1] G. Kresse and J. Furthmüller, Efficient iterative schemes for ab initio total-energy calculations using a plane-wave basis set, *Phys. Rev. B* **54**, 11169 (1996).
 - [2] G. Kresse and J. Furthmüller, Efficiency of ab-initio total energy calculations for metals and semiconductors using a plane-wave basis set, *Comp. Mater. Sci.* **6**, 15 (1996).
 - [3] J. P. Perdew, K. Burke, and M. Ernzerhof, Generalized Gradient Approximation Made Simple, *Phys. Rev. Lett.* **77**, 3865 (1996).
 - [4] H. J. Monkhorst and J. D. Pack, Special points for brillouin-zone integrations, *Phys. Rev. B* **13**, 5188 (1976).
 - [5] V. I. Anisimov, J. Zaanen, and O. K. Andersen, Band theory and Mott insulators: Hubbard U instead of Stoner I, *Phys. Rev. B* **44**, 943 (1991).
 - [6] S. L. Dudarev, G. A. Botton, S. Y. Savrasov, C. J. Humphreys, and A. P. Sutton, Electron-energy-loss spectra and the structural stability of nickel oxide: An LSDA+U study, *Phys. Rev. B* **57**, 1505 (1998).
 - [7] A. A. Mostofi, J. R. Yates, Y.-S. Lee, I. Souza, D. Vanderbilt, and N. Marzari, Wannier90: A tool for obtaining maximally-localised Wannier functions, *Computer Physics Communications* **178**, 685 (2008).
 - [8] A. A. Mostofi, J. R. Yates, G. Pizzi, Y.-S. Lee, I. Souza, D. Vanderbilt, and N. Marzari, An updated version of wannier90: A tool for obtaining maximally-localised Wannier functions, *Computer Physics Communications* **185**, 2309 (2014).